First triple-wavelength lidar observations of depolarization and extinction-to-backscatter ratios of Saharan dust

Moritz Haarig[1], Albert Ansmann[1], Ronny Engelmann[1], Holger Baars[1], Dietrich Althausen[1], Carlos Toledano[2], Benjamin Torres[3], Martin Radenz[1], and Ulla Wandinger[1]

[1]Leibniz Institute for Tropospheric Research, Leipzig, Germany
[2]Atmospheric Optics Group, University of Valladolid, Valladolid, Spain
[3]Laboratoire d'Optique Atmosphérique, Université des Sciences et Technologies de Lille, Villeneuve d'Ascq, France

Correspondence: Moritz Haarig (haarig@tropos.de)

Abstract. Two Saharan dust layers observed over Leipzig, Germany, in February and March 2021 were used to provide the first ever lidar measurements of the dust lidar ratio (extinction-to-backscatter ratio) and linear depolarization ratio at all three classical lidar wavelengths (355, 532 and 1064 nm). The pure dust conditions during the first event exhibit lidar ratios of 47±8, 50±5 and 63±13 sr and particle linear depolarization ratios of 0.260±0.026, 0.298±0.017 and 0.214±0.025 at the wavelengths of 355, 532 and 1064 nm, respectively. The second, slightly polluted dust case shows a similar spectral behavior of the lidar and depolarization ratios with values of the lidar ratio of 52±8, 47±5 and 61±10 sr and the depolarization ratio of 0.188±0.053, 0.270±0.017 and 0.242±0.007 at 355, 532 and 1064 nm, respectively. The results were compared with AERONET v3 inversion solutions and GRASP retrievals at six and seven wavelengths. Both retrieval schemes make use of a spheroidal dust shape model. The spectral slope of the lidar ratio from 532 to 1064 nm could be well reproduced by the AERONET and GRASP retrieval schemes. However, significant differences between the measured and retrieved wavelength dependence of the particle linear depolarization ratio were found. The discrepancies are especially large for the 1064 nm depolarization ratio in the case of the AERONET computations. The potential sources for these uncertainties are discussed.

1 Introduction

Triple-wavelength polarization Raman lidar observations of particle depolarization and extinction-to-backscatter ratios are of importance for several reasons. Many lidars (including ceilometers) are standard backscatter lidars and need trustworthy information about the particle extinction-to-backscatter ratio (lidar ratio) in the retrieval of backscatter and extinction profiles and aerosol optical thickness (AOT). This is of special importance in the case of the spaceborne CALIPSO lidar (Cloud-Aerosol Lidar and Infrared Pathfinder Satellite Observations) monitoring aerosols and clouds around the globe at 532 and 1064 nm (Omar et al., 2009; Kim et al., 2018). There are several CALIPSO lidar studies focusing on desert dust (e.g., Amiridis et al., 2013; Marinou et al., 2017). Dust is besides marine aerosol the most important natural aerosol type in the atmosphere. Dust and non-dust aerosol components can be easily separated by means of depolarization ratio observations (Tesche et al., 2009a; Mamouri and Ansmann, 2017). Triple-wavelength lidar measurements are also of importance for aerosol typing efforts that make use of spectrally resolved intensive aerosol parameters such as the linear depolarization ratio, extinction-to-backscatter

ratio, as well as the extinction and backscatter-related Ångström exponents for all climate-relevant aerosol types (marine, dust,

25 smoke, volcanic, and haze particles) (Burton et al., 2012; Groß et al., 2013; Baars et al., 2017). In this respect, our measurements will contribute to these aerosol typing efforts by adding new information on dust lidar and depolarization ratios at 1064 nm.

The most important aspect of triple-wavelength lidar observations of dust depolarization and lidar ratios is, however, that such measurements at all three classical aerosol lidar wavelengths (355, 532,and 1064 nm) are required to improve optical models applied to simulate the optical properties of aerosol particles as a function of size distribution, shape characteristics,

30 and chemical composition. Especially in the case of mineral dust there is a strong request for those lidar observations to improve the applied particle shape parameterization. These data, presented here, will support the validation of shape models for the irregularly shaped dust particles. The particle depolarization ratio sensitively depends on the form of the backscattering particles, whereas the dust lidar ratio is a function of particle shape as well as of the mineralogical composition of the dust particles (Schuster et al., 2012; Shin et al., 2018)

35 Modeling of dust optical properties is especially challenging for the 180° backscattering direction. Complex dust shape models were developed to improve the agreement between lidar observations and respective simulation results (Gasteiger et al., 2011; Kemppinen et al., 2015; Saito et al., 2021). The spheroidal shape model is widely used (Dubovik et al., 2006), e.g., in the analysis of Aerosol Robotic Network (AERONET) sun and sky radiometer measurements to obtain the inversion products (Sinyuk et al., 2020) which include the lidar ratio and the particle linear depolarization ratio at four wavelengths between 440

40 and 1020 nm. These retrieval products were compared with lidar measurements of desert dust (Tesche et al., 2009b; Müller et al., 2010, 2012; Noh et al., 2017; Shin et al., 2018; Toledano et al., 2019) and partly large discrepancies were found. Triple-wavelength lidar observations of the depolarization ratio are available since 2013 (Burton et al., 2015; Haarig et al., 2017). However, direct observations of the lidar ratio at all three lidar wavelengths are missing as were stated in Shin et al. (2018).

Haarig et al. (2016) showed, for the first time, directly measured vertical profiles of the 1064 nm extinction coefficient. Since

45 then, we used the triple-wavelength Raman lidar approach to characterize cirrus (Haarig et al., 2016) and wildfire smoke (Haarig et al., 2018) in terms of backscatter, extinction, lidar ratio, and depolarization ratio at 355, 532 and 1064 nm. Now, we present two case studies of pure dust and polluted dust outbreaks towards central Europe which occurred in February and March 2021. The first Saharan dust plume extended from the ground up to 8 km height and reached our station in Leipzig, Germany, in less than 2 days (around 36 hours) after emission. This fast transport process at great heights prevented mixing

50 with anthropogenic pollution. The second dust outbreak occurred one week later. The dust spent more time over Europe (3–4 days of transport) and the dust plume mixed with European haze.

The article is structured as follows. After a short description of the lidar system and the additional, new option to measure extinction coefficients at 1064 nm in Sect. 2, the two observed dust cases are presented in Sect. 3. The discussion in Sect. 4 focuses on the spectral dependence of the depolarization ratio and lidar ratio. We use the opportunity to compare our results

55 with AERONET v3 inversion results as well as with products obtained by applying the Generalized Retrieval of Aerosol and Surface Properties (GRASP) technique (Torres et al., 2017), available for the same dust event in February 2021.

2 Instrumentation

For the present study two lidars and an AEROENT sun photometer at the Leibniz Institute for Tropospheric Research (TRO-POS) in Leipzig (51.35°N , 12.43°E), Germany, were used. The multiwavelength polarization Raman lidar BERTHA (Backscat-

60 ter Extinction lidar-Ratio Temperature Humidity profiling Apparatus, Haarig et al., 2017) provides the backscatter coefficient, extinction coefficient and depolarization ratio at 355, 532 and 1064 nm (3+3+3 configuration). However, it can not measure the depolarization ratio and the extinction coefficient at 1064 nm at the same time. A couple of minutes are necessary to switch the NIR setup from depolarization to extinction measurements. The extinction coefficients at 355 and 532 nm were derived by using the vibrational-rotational Raman backscattering channels at 387 and 607 nm, respectively. The rotational Raman tech-

65 nique (Whiteman, 2003a, b; Veselovskii et al., 2015; Haarig et al., 2016) was applied to provide measurements of the extinction coefficient at 1064 nm. This Raman channel is equipped with an interference filter centered at about 1058 nm (Alluxa, Santa Rosa, CA, http://www.alluxa.com). The transmission band is from 1053 to 1062 nm with a transmission >90% in this wavelength range. For the laser wavelength of 1064.14 nm, the transmission is specified to be 0.005%. For a better suppression of the transmitted layer radiation at 1064 nm two 1058 nm interference filters are used in front of the photomultiplier tube (pho-

70 tocounting, R3236 from Hamamatsu, Japan). The filter width of 9 nm restricts the 1058 nm Raman observations to nighttime hours. More details can be found in Haarig et al. (2016).

Linearly polarized laser pulses are transmitted into the atmosphere and the so-called co-polarized and cross-polarized signal components are measured. "Co" and "cross" denote the planes of polarization parallel and orthogonal to the plane of linear polarization of the transmitted laser pulses, respectively. In the case of spherical droplets, wet marine and small haze particles,

75 the polarization state of the laser pulse radiation is preserved during the backscattering process and the particle linear depolarization ratio PLDR, computed from the ratio of the cross-polarized to the co-polarized signal component, is close to zero. In the case of irregularly shaped dust particles, strong depolarization takes place during the backscattering event and the PLDR values are close to 0.3 at 532 nm (Freudenthaler et al., 2009; Haarig et al., 2017). The calibration of the polarization-sensitive channels at all three wavelengths makes use of the so-called $\Delta 90°$ method (Freudenthaler, 2016). The error estimation is de-

80 scribed in Haarig et al. (2017). The 3+3+3 configuration has already been successfully applied in the case of an extreme event of wildfire smoke in the stratosphere (Haarig et al., 2018).

The second lidar used in this study is the Arielle Polly[XT] (POrtabLe Lidar sYstem, neXT generation) (Engelmann et al., 2016). The Arielle lidar was operated several meters apart from the BERTHA instrument. The Arielle lidar has been recently deployed on the research vessel Polarstern in the central Arctic (Engelmann et al., 2020).

85 A CIMEL sun-sky photometer of AEROENT (Holben et al., 1998) is operated at Leipzig since 2000. Currently, only level 1.5 data are available for February and March 2021, although the data already passed all quality criteria, including cloud screening and operational checks (Giles et al., 2019). Besides the standard AERONET data analysis procedure (Sinyuk et al., 2020), the GRASP retrieval scheme using optical information at six and seven AERONET wavelengths was applied (Dubovik et al., 2014; Torres et al., 2017; Toledano et al., 2019) in order to derive lidar ratio and depolarization ratio values.

3 Observations

Two case studies of triple-wavelength depolarization ratio and lidar ratio observations of Saharan dust from late winter 2021 will be shown. Pure dust conditions were observed on 22–23 February 2021, while mixed pollution-dust conditions prevailed on 3 March 2021.

3.1 First dust outbreak: 22–23 February 2021

Huge amounts of mineral dust were emitted from western Saharan regions around and before 21 February 2021. The dust plumes were directly transported towards central Europe and reached Leipzig in less than 2 days (around 36 hours) after emission as shown by the HYSPLIT (HYbrid Single-Particle Lagrangian Integrated Trajectory) backward trajectories (Stein et al., 2015) in Figure 1b. More detailed source attributions indicate the Sahara as main source region for the lofted layers (see Fig. 2). Below 3 km height, aerosol from continental Europe were probably mixed into the Saharan dust plumes. In the night of 22–23 February 2021, the dust plumes reached from the ground up to 8 km height. Saharan dust was transported towards central Europe continuously from the evening of 22 February till the morning of 26 February 2021. The transport pattern were similar to the dust outbreak in October 2001 described in Ansmann et al. (2003), which was measured by the entire EARLINET community (European Aerosol Research LIdar NETwork, now part of the Aerosol, Clouds and Trace Gases Research Infrastructure, ACTRIS) (Pappalardo et al., 2014).

The lidar measurements are presented in Fig. 1. The time-height plot (Fig. 1a) of the cross-polarized and range-corrected signal at 532 nm provides an overview of the dust conditions observed with the BERTHA lidar system. During the first 20 min the system was in the configuration to measure the depolarization ratio at 1064 nm. Then, the configuration was switched to permit measurements of the extinction coefficient at 1064 nm for the next 2 h 15 min. Some clouds were forming in the humid dust layer at around 4 km height, indicated by strong backscatter signals (dark red) and the attenuation of laser radiation above the cloud layers. The cloud-containing profiles were excluded from the calculation of the dust optical properties. The signals at 355 nm of the BERTHA lidar were very weak during that night. Therefore, the optical properties at 355 nm were taken from the nearby Arielle Polly^{XT} measurements. Additionally, the optical properties at 532 nm measured with the Arielle system are shown in Fig. 1c–e. The profiles at 532 nm (green lines) from the different lidar observations agree well. Above the dust layers, small cirrus clouds at 10–11 km height could be used to check the correct reference value settings for the backscatter coefficients, especially at 1064 nm. The ice crystals are large compared to laser wavelengths leading to a wavelength-independent backscatter coefficient within the cirrus layers.

For the thickest part of the dust layer (3–4 km height), no wavelength dependence for the backscatter coefficient (backscatter Ångström exponent AE_β=0.061±0.193 in the 355-1064 nm wavelength range) was found. Above, a decrease in the backscatter coefficient towards 1064 nm (AE_β=0.792±0.260 in the 532-1064 nm wavelength range) was observed. The definition of the Ångström exponent is given in Sect. 4. The extinction coefficient exceeded 100 Mm^{-1} at around 3.5 km height at all three wavelengths. The lidar ratio (Fig. 1e) derived in the strongest part of the dust layer (3–5 km height), increased with wavelength from 47±8 sr at 355 nm, to 50±5 sr at 532 nm and 63±13 sr at 1064 nm. The particle linear depolarization ratio PLDR at

532 nm of up to 0.30±0.02 (3–5 km layer mean and systematic uncertainty) indicates pure dust conditions (Freudenthaler et al., 2009). The PLDR decreases towards 355 nm (0.260±0.026) and 1064 nm (0.214±0.025). Note again, that the PLDR
125 at 1064 nm was measured during the first 20 min (22:12–22:32 UTC), whereas all other intensive optical properties were measured from 22:45–01:02 UTC. A summary of the intensive optical properties measured in the night of 22–23 February 2021 can be found in Table 1.

The AERONET version 3 inversion results for the lidar ratio and PLDR (five separate observations) performed on 23 February 2021 between 11:35 and 14:49 UTC are compared with the lidar observations in Section 4. The AERONET measurement
130 period is indicated in Fig. 2. The continuous observations of the Arielle lidar and the source attribution for 23 February 2021 in Fig. 2 reveal that the same Saharan dust layer was present during the nighttime lidar measurements and the daytime AERONET observations.

3.2   Second dust outbreak: 3 March 2021

A second dust outbreak occurred one week later on 3 March 2021. Travel time was 3–4 days from the Sahara to Leipzig
135 via Spain and France as indicated by the HYSPLIT backward trajectories in Fig 3b. This time the BERTHA lidar was fully operational at all three wavelengths so that also the optical properties at 355 nm could be used. The lidar observations are shown in Fig. 3. The dust layers extended up to 5 km in the beginning, later on the dust plumes descended down to 4 km height. During the first 20 min, the lidar was in the configuration to measure the depolarization ratio at 1064 nm (3+2+3 configuration). The process of changing the interference and depolarization filters was optimized so that 7 min later the extinction measurement at
140 1064 nm could be started (3+3+2 configuration). To obtain trustworthy extinction values at 1064 nm, signal profiles collected over 3 h 20 min (21:11 – 00:32 UTC) were averaged. The main dust layer extended from 1.5 – 4 km height and provided vertically homogeneous conditions for averaging. The profiles of the extinction coefficients and lidar ratios in Fig. 3d and e are shown for a sliding average window length of 742.5 m.

The cirrus clouds at 8.5–10.5 km height were again used to check the settings of the reference values for the backscatter
145 coefficients. In this way, the spectral slope of the backscatter coefficient within the dust layer was constrained. As found in other observations of mineral dust (Haarig et al., 2017; Hofer et al., 2017; Veselovskii et al., 2016), the backscatter coefficients at 355 and 532 nm were almost the same, whereas values at 1064 nm were lower (around 80% of the value at 532 nm). The lidar ratio at 1064 nm (61±10 sr) was slightly higher than at 532 nm (47±5 sr). The slight increase in the lidar ratio at 355 nm (52±8 sr) compared to 532 nm is an indication for pollution mixed into the dust layer.
150 The depolarization ratios (Fig. 3f) at 355 and 532 nm were measured from 21:11 – 00:32 UTC, while the depolarization ratio at 1064 nm was observed from 20:44 – 21:04 UTC. The dust layer showed a larger vertical extend up to 5 km height during the first shorter measurement period. For comparison the PLDR at 532 nm from the first measurement is shown as a dashed green line and used to derive the ratio of PLDR (1064/532) in Table 1. The depolarization ratios (0.270±0.017 at 532 nm) were a bit lower than on 22–23 February (pure dust conditions). The longer transport way over Europe obviously caused the weak
155 mixing with anthropogenic pollution. Especially, the PLDR at 355 nm was significantly reduced (about 0.19) compared to the pure dust values around 0.26.

A summary of the intensive optical properties measured on 3 March 2021 can be found in Table 1. Unfortunately, no AERONET observations are available for 3 March 2021. Most of the time, extended cirrus layers prevented sun photometer observations.

4 Discussion

160 ### 4.1 Spectral dependence of the lidar ratio

The discussion of the spectral behavior of the lidar ratio of Saharan dust is based on the two presented Leipzig case studies and observations on Barbados during the Saharan Aerosol Long-range Transport and Aerosol–Cloud-Interaction Experiment (SALTRACE, Weinzierl et al., 2017). The BERTHA lidar system on Barbados (13°N, 59°W) measured the Saharan dust after long-range transport over 5000 – 8000 km across the Atlantic Ocean in three intensive campaigns in 2013 and 2014

165 (Haarig et al., 2017). The statistics of the lidar ratio at 355 and 532 nm and the Ångström exponents based on 22 SALTRACE measurement cases are summarized in Table 1. During the SALTRACE campaigns, the rotational Raman technique applied to measure the extinction at 1064 nm was not implemented in the BERTHA lidar. However, the lidar ratio at 1064 nm could be estimated for one intense dust event with very constant dust conditions observed on 20 June 2014. Here, the column-integrated backscatter coefficient at 1064 nm in the dust layer after sunset and the AOT at 1020 nm (from AERONET observations) before

170 sunset were used as described in Mamouri and Ansmann (2017). An AOT contribution of 0.035 for marine aerosol below the dust layer was subtracted to obtain the pure dust value for the lidar ratio estimate. This method led to a dust lidar ratio of 67±15 sr at 1064 nm.

The spectral dependence of the lidar ratio of Saharan dust is shown in Fig. 4a. The lidar ratio does not change significantly in the wavelength range of 355 to 532 nm. In the case of Saharan dust, this was observed in numerous studies (e.g., Tesche

175 et al., 2011; Groß et al., 2015). Some studies however, point to higher values in the UV (Mattis et al., 2002). Veselovskii et al. (2020) observed cases with the same lidar ratio at 355 and 532 nm and cases with higher lidar ratios at 355 nm. The ratio of lidar ratios for 355 and 532 nm can be an indicator of the imaginary refractive index enhancement in the UV depending on the mineralogical composition of the dust particles (Veselovskii et al., 2020).

The present study provides clear evidence for an increase of the lidar ratio from 532 to 1064 nm. As mentioned, the reason

180 is the lower particle backscatter coefficient β at 1064 nm compared to the one at 532 nm so that the backscatter Ångström exponent AE_β, defined as $AE_{\beta,\lambda_i,\lambda_j} = \ln(\beta_i/\beta_j)/\ln(\lambda_j/\lambda_i)$ in the spectral range from wavelength λ_i to λ_j, is positive. The extinction coefficient α usually does not show a significant wavelength dependence so that the respective extinction Ångström exponent AE_α is close to zero. According to Ansmann et al. (2002), the Ångström exponent AE_S for the lidar ratio S, given by

185 $$AE_S = AE_\alpha - AE_\beta,\qquad\qquad(1)$$

is then negative. This relationship (1) holds within the uncertainties for the intensive optical properties provided in Table 1. The ratios of the lidar ratios given in Table 1 corroborate the increase of the lidar ratio from 532 to 1064 nm. We found around 26–31% higher values for the lidar ratio at 1064 nm compared to 532 nm. Combined sun photometer and lidar observations

during the Saharan Mineral Dust Experiments (SAMUM) in Morocco led to the conclusion that the lidar ratio is almost in-

190   dependent of wavelength with values of 55±5 sr, 56±5 sr, and 59±7 sr at 355, 532, 1064 nm, respectively (Tesche et al., 2009b). The authors used the extinction-related Ångström exponent (for the 500-1020 nm wavelength range) from sun photometer observations to transfer the extinction profile from 532 to 1064 nm and calculate the lidar ratio at 1064 nm using the corresponding backscatter profile in addition. Now, in the late winter of 2021, we found lidar ratio values of 47±8 sr, 50±5 sr, and 63±13 sr for the three wavelengths.

195   The spectral dependence of the lidar ratio measured with lidar and retrieved from the AERONET observations are compared in Fig. 4b. The AERONET data base (AERONET, 2021) provides AOT values at 440, 675, 870 and 1020 nm together with further products such as lidar ratio and linear depolarization ratio. The lidar ratio and particle linear depolarization ratio are retrieved by means of the AERONET v3 inversion algorithm (Giles et al., 2019; Sinyuk et al., 2020) which assumes a spheroidal dust particle shape (Dubovik et al., 2006). Additionally to the standard four wavelengths, the inversion has been performed using

200   the GRASP algorithm at six wavelengths (plus 500 and 1640 nm) and seven wavelengths (plus 380 nm, Torres et al., 2017). For the mean values the data were filtered in the way that the residual is <10% of the inversion retrieval. A comparison of the lidar observations with the respective AERONET v3 inversion products was only possible on 22–23 February 2021.

The spectral slope of the lidar ratio is well reproduced by the AERONET observations for the spectral range from 675 to 1020 nm. The four- and six-wavelength mean values show exactly the same spectral slope as obtained by the lidar observa-

205   tions. The retrieved lidar ratios at 440 nm using the standard AERONET algorithm indicate an overestimation of the lidar ratio in the UV range. The GRASP retrieval at 440 nm shows a much better agreement with the lidar observations. The increase of the lidar ratio at 380 nm (seven-wavelength retrieval) points again to an overestimation of the lidar ratio in the UV range. The enhanced lidar ratios in the UV retrieved by AERONET were already discussed by Shin et al. (2018): The drop of the imaginary part of the refractive index at 440 nm compared to 675 nm is too strong in the AERONET inversion procedure,

210   resulting in too high lidar ratios at 440 nm. In-situ studies could not confirm the spectral slope of the imaginary part used in AERONET inversions as discussed by Müller et al. (2012). As mentioned, the imaginary part of the refractive index depends on the mineralogical composition of dust particles. This changes for different dust source regions. Schuster et al. (2012) investigated the variation of the lidar ratio obtained from AERONET observations for different deserts around the Earth and found significant differences. The highest lidar ratios were found for the western Sahara, lower values for Asian deserts. The global

215   coverage of AERONET sun photometers is a big advantage. However, the retrievals should be checked against Raman or high spectral resolution lidar (HSRL) observations as has been started by Shin et al. (2018). Another source of uncertainty is always the boundary layer (at Leipzig and elsewhere outside the deserts). The fine-mode aerosol pollution can significantly influence the AERONET lidar-ratio products, especially at the wavelength of 440 nm.

4.1.1   Spectral dependence of the depolarization ratio

220   The spectral dependence of the particle linear depolarization ratio of Saharan dust is shown in Fig. 5a. The results of the two presented case studies are set into context with previous triple-wavelength depolarization ratio observations. The observations of Saharan dust close to the source in Morocco (Freudenthaler et al., 2009) and after long-range transport towards Barbados

(Haarig et al., 2017) and North America (Burton et al., 2015) show a consistent spectral slope. The PLDR increases in the wavelength range from 355 to 532 nm and then decreases again towards the wavelength of 1064 nm. Table 1 summarizes the
225 spectral dependence of the PLDR. The table includes the ratio of PLDR for the wavelength pairs of 355 and 532 nm and of 1064 and 532 nm for the two presented cases studies at Leipzig and the SALTRACE observations. The depolarization ratio at 355 nm was very low on 3 March 2021 (0.188±0.053) and probably reflects the impact of aerosol pollution mixed into the dust layers. The small and spherical pollution particles affect the backscattering at shorter wavelengths more effectively than at the longer wavelengths. For pure Saharan dust (22–23 February 2021, Barbados, Morocco), the PLDR at 355 nm reached
230 around 84–90% of the value at 532 nm. The PLDR at 1064 nm depends on the amount of rather large dust particles in the observed layer and thus is very sensitive to the travel duration (and the corresponding removal of large particles). The decrease of the PLDR with wavelength in the range from 532 to 1064 nm is expressed by PLDR ratios of 0.7 – 0.9 for Saharan dust after long-range transport (Table 1).

The spectral slope of the PLDR is not an unique feature of Saharan dust. Hu et al. (2020) observed the same spectral dependence
235 but with generally higher values for dust from the Taklamakan desert in western China very close to the main dust sources, and thus with an enhanced fraction of very large dust particles. The same behavior was found for locally emitted dust in the Southwest of the United States (Burton et al., 2015). The large dust particles of the freshly emitted dust were still present in the air during the lidar observations and produced significantly higher depolarization ratios of 0.38±0.01 at 1064 nm.

The spectral dependence of the PLDR in Fig. 5b derived from the sun and sky photometer observations is very different
240 from the respective lidar observations of the PLDR spectral behavior. The lidar measurements of desert dust generally show a pronounced maximum of the depolarization ratio at 532 nm. This is not visible in the AERONET spectra. By using the GRASP method (including the use of optical data measured at 1640 nm, not shown in the figure) leads to a decrease of the PLDR with wavelength, starting already at 1020 nm. However, the PLDR in the NIR is still overestimated for the presented case, in which a lower PLDR at 1064 nm was measured. The six- and seven-wavelength GRASP retrievals lead to a better agreement in
245 the NIR, but underestimates the depolarization ratio at the shorter wavelengths. Previous comparisons of lidar-measured and AERONET-retrieved depolarization ratios pointed out that the spheroidal model used for the AERONET inversions fails to predict the spectral slope of the PLDR (Noh et al., 2017; Shin et al., 2018). Only Toledano et al. (2019) was able to obtain the spectral slope as observed with polarization lidar systems by using the six-wavelength sun photometer retrieval for Saharan dust observations on Barbados during SALTRACE. In their study, the PLDR increases from 0.277±0.040 at 440 nm to 0.282±0.031
250 at 675 nm and then decreases again to 0.259±0.030 at 1020 nm. A further decrease was retrieved for the wavelength of 1640 nm (0.191±0.028). Again, the boundary-layer fine-mode pollution (over Leipzig) is a source of uncertainty in the AERONET retrievals and may lead to smaller AERONET depolarization ratio values than observed with lidar in the lofted dust layer. However, the significant discrepancies between the AERONET and the lidar observations in the 532–1064 nm spectral range remain an unsolved issue and seem to be related to the used spheroidal shape model in the AERONET and GRASP retrieval
255 schemes.

5 Conclusions

We presented, for the first time, measurements of the dust lidar ratio at the main aerosol lidar wavelengths of 355, 532 and 1064 nm. Together with the depolarization ratio at these wavelengths, we demonstrated the unique potential of a triple-wavelength polarization Raman lidar to permit so-called 3+3+3 profiling (3 backscatter coefficients, 3 extinction coefficients, 3 depolarization ratios). Two case studies of Saharan dust over central Europe were presented, one for pure dust conditions and another case with slightly polluted dust. The measurement of the depolarization ratio and lidar ratio at three wavelengths from the UV to the NIR provides an improved, more complete set of constraints in modeling efforts to develop a realistic dust particle shape model. A better assessment of the absorption properties which are linked to the mineralogical composition of the dust particles may be possible by considering the spectral information of the lidar ratio from the UV to the NIR. Nevertheless, realistic assumptions on the imaginary part of the refractive index are required. Good measurements of the refractive index are important to allow for an accurate computation of the spectral slope of the lidar ratio in the wavelength range from 355 to 1064 nm. It would be desirable, in this context, to perform such triple-wavelength lidar measurements in very different desert regions of the world. Middle East and central Asian dust show, e.g., lower lidar ratios, especially at 532 nm, as presented here (Hofer et al., 2020). We found lidar ratios of 47±8, 50±5 and 63±13 sr at 355, 532 and 1064 nm, respectively, for pure dust conditions, and respective lidar ratios of 52±8, 47±5 and 61±10 sr for slightly polluted dust. In central Asia, pure dust lidar ratios were on average 43±3 and 39±4 sr at 355 and 532 nm, respectively (Hofer et al., 2020).

The comparison with AERONET v3 inversion products revealed that the spectral dependence of PLDR was not matched by the AERONET results. The GRASP computations based on the optical information measured at six and seven wavelengths improved the agreement, but lead to overall lower values. However, the spectral slope of the lidar ratio from the VIS towards the NIR was retrieved well by the AERONET and the GRASP data analysis. Problems remain in the 355-532 nm spectral range. The retrievals at four (AERONET) and seven wavelengths (GRASP) led to an overestimation of the lidar ratio at the short wavelengths. We may conclude that an appropriate particle shape model for the non-spherical dust particles is still missing. The spheroidal shape model (Dubovik et al., 2006) has proven to be useful to derive volume and surface area concentrations from sky radiance and AOT observations at several wavelengths. However, this shape model is not able to reproduce the spectral slope of the particle linear depolarization ratio measured with lidar at the 180°backscatter direction. Complex particle-shape models (Gasteiger et al., 2011; Kemppinen et al., 2015; Saito et al., 2021) are computationally expensive. Nevertheless, they may lead to a more realistic representation of the non-spherical dust particles in the models.

As a final remark, it would be helpful, and a good addition to field observations, if laboratory measurements of the depolarization and lidar ratios at all three wavelengths (in the 180°backscatter direction) could be realized for well defined size fractions of real dust particles with real irregular shape characteristics. An effort was already started by Miffre et al. (2016).

Data availability. The BERTHA lidar data can be obtained upon request. The Arielle data are available in the PollyNET data base (https://polly.tropos.de/). (PollyNET, 2021). The AERONET data are available via the AERONET web page (https://aeronet.gsfc.nasa.gov/) under the site 'Leipzig' (AERONET, 2021).

290 *Author contributions.* MH performed the lidar measurements, analyzed the data and wrote the manuscript. AA provided advise and valuable comments on the manuscript. RE supported the rotational Raman measurements. HB provided the Arielle results. DA provided technical support for the BERTHA lidar system. CT and BT provided the six and seven wavelength GRASP retrieval. MR did the source appointment analysis. UW provided comments on light scattering.

Competing interests. The authors declare that they have no conflict of interest.

References

AERONET(2021): AErosol RObotic NETwork, aerosol data base, available at: https://aeronet.gsfc.nasa.gov/, last access: 22 June, 2021.

Amiridis, V., Wandinger, U., Marinou, E., Giannakaki, E., Tsekeri, A., Basart, S., Kazadzis, S., Gkikas, A., Taylor, M., Baldasano, J., and Ansmann, A.: Optimizing CALIPSO Saharan dust retrievals, Atmospheric Chemistry and Physics, 13, 12 089–12 106, https://doi.org/10.5194/acp-13-12089-2013, 2013.

Ansmann, A., Wagner, F., Müller, D., Althausen, D., Herber, A., von Hoyningen-Huene, W., and Wandinger, U.: European pollution outbreaks during ACE 2: Optical particle properties inferred from multiwavelength lidar and star-Sun photometry, Journal of Geophysical Research: Atmospheres, 107, AAC 8–1–AAC 8–14, https://doi.org/10.1029/2001JD001109, 2002.

Ansmann, A., Bösenberg, J., Chaikovsky, A., Comerón, A., Eckhardt, S., Eixmann, R., Freudenthaler, V., Ginoux, P., Komguem, L., Linné, H., Márquez, M. A. L., Matthias, V., Mattis, I., Mitev, V., Müller, D., Music, S., Nickovic, S., Pelon, J., Sauvage, L., Sobolewsky, P., Srivastava, M. K., Stohl, A., Torres, O., Vaughan, G., Wandinger, U., and Wiegner, M.: Long-range transport of Saharan dust to northern Europe: The 11–16 October 2001 outbreak observed with EARLINET, Journal of Geophysical Research: Atmospheres, 108, 4783, https://doi.org/10.1029/2003JD003757, 2003.

Baars, H., Seifert, P., Engelmann, R., and Wandinger, U.: Target categorization of aerosol and clouds by continuous multiwavelength-polarization lidar measurements, Atmospheric Measurement Techniques, 10, 3175–3201, https://doi.org/10.5194/amt-10-3175-2017, 2017.

Burton, S. P., Ferrare, R. A., Hostetler, C. A., Hair, J. W., Rogers, R. R., Obland, M. D., Butler, C. F., Cook, A. L., Harper, D. B., and Froyd, K. D.: Aerosol classification using airborne High Spectral Resolution Lidar measurements – methodology and examples, Atmospheric Measurement Techniques, 5, 73–98, https://doi.org/10.5194/amt-5-73-2012, 2012.

Burton, S. P., Hair, J. W., Kahnert, M., Ferrare, R. A., Hostetler, C. A., Cook, A. L., Harper, D. B., Berkoff, T. A., Seaman, S. T., Collins, J. E., Fenn, M. A., and Rogers, R. R.: Observations of the spectral dependence of linear particle depolarization ratio of aerosols using NASA Langley airborne High Spectral Resolution Lidar, Atmospheric Chemistry and Physics, 15, 13 453–13 473, https://doi.org/10.5194/acp-15-13453-2015, 2015.

Dubovik, O., Sinyuk, A., Lapyonok, T., Holben, B. N., Mishchenko, M., Yang, P., Eck, T. F., Volten, H., Muñoz, O., Veihelmann, B., van der Zande, W. J., Leon, J.-F., Sorokin, M., and Slutsker, I.: Application of spheroid models to account for aerosol particle nonsphericity in remote sensing of desert dust, Journal of Geophysical Research: Atmospheres, 111, D11 208, https://doi.org/10.1029/2005JD006619, 2006.

Dubovik, O., Lapyonok, T., Litvinov, P., Herman, M., Fuertes, D., Ducos, F., Lopatin, A., Chaikovsky, A., Torres, B., Derimian, Y., Huang, X., Aspetsberger, M., and Federspiel, C.: GRASP: a versatile algorithm for characterizing the atmosphere, SPIE: Newsroom, https://doi.org/doi:10.1117/2.1201408.005558, 2014.

Engelmann, R., Kanitz, T., Baars, H., Heese, B., Althausen, D., Skupin, A., Wandinger, U., Komppula, M., Stachlewska, I. S., Amiridis, V., Marinou, E., Mattis, I., Linné, H., and Ansmann, A.: The automated multiwavelength Raman polarization and water-vapor lidar PollyXT: the neXT generation, Atmospheric Measurement Techniques, 9, 1767–1784, https://doi.org/10.5194/amt-9-1767-2016, 2016.

Engelmann, R., Ansmann, A., Ohneiser, K., Griesche, H., Radenz, M., Hofer, J., Althausen, D., Dahlke, S., Maturilli, M., Veselovskii, I., Jimenez, C., Wiesen, R., Baars, H., Bühl, J., Gebauer, H., Haarig, M., Seifert, P., Wandinger, U., and Macke, A.: UTLS wildfire smoke over the North Pole region, Arctic haze, and aerosol-cloud interaction during MOSAiC 2019/20: An introductory, Atmospheric Chemistry and Physics Discussions, 2020, 1–41, https://doi.org/10.5194/acp-2020-1271, 2020.

Freudenthaler, V.: About the effects of polarising optics on lidar signals and the Δ 90 calibration, Atmospheric Measurement Techniques, 9, 4181–4255, https://doi.org/10.5194/amt-9-4181-2016, 2016.

Freudenthaler, V., Esselborn, M., Wiegner, M., Heese, B., Tesche, M., Ansmann, A., Müller, D., Althausen, D., Wirth, M., Fix, A., Ehret, G., Knippertz, P., Toledano, C., Gasteiger, J., Garhammer, M., and Seefeldner, M.: Depolarization ratio profiling at several wavelengths in pure Saharan dust during SAMUM 2006, Tellus B, 61, 165–179, https://doi.org/10.1111/j.1600-0889.2008.00396.x, 2009.

Gasteiger, J., Wiegner, M., Groß, S., Freudenthaler, V., Toledano, C., Tesche, M., and Kandler, K.: Modelling lidar-relevant optical properties of complex mineral dust aerosols, Tellus B, 63, 725–741, https://doi.org/10.1111/j.1600-0889.2011.00559.x, 2011.

Giles, D. M., Sinyuk, A., Sorokin, M. G., Schafer, J. S., Smirnov, A., Slutsker, I., Eck, T. F., Holben, B. N., Lewis, J. R., Campbell, J. R., Welton, E. J., Korkin, S. V., and Lyapustin, A. I.: Advancements in the Aerosol Robotic Network (AERONET) Version 3 database – automated near-real-time quality control algorithm with improved cloud screening for Sun photometer aerosol optical depth (AOD) measurements, Atmospheric Measurement Techniques, 12, 169–209, https://doi.org/10.5194/amt-12-169-2019, 2019.

Groß, S., Esselborn, M., Weinzierl, B., Wirth, M., Fix, A., and Petzold, A.: Aerosol classification by airborne high spectral resolution lidar observations, Atmospheric Chemistry and Physics, 13, 2487–2505, https://doi.org/10.5194/acp-13-2487-2013, 2013.

Groß, S., Freudenthaler, V., Schepanski, K., Toledano, C., Schäfler, A., Ansmann, A., and Weinzierl, B.: Optical properties of long-range transported Saharan dust over Barbados as measured by dual-wavelength depolarization Raman lidar measurements, Atmospheric Chemistry and Physics, 15, 11 067–11 080, https://doi.org/10.5194/acp-15-11067-2015, 2015.

Haarig, M., Engelmann, R., Ansmann, A., Veselovskii, I., Whiteman, D. N., and Althausen, D.: 1064 nm rotational Raman lidar for particle extinction and lidar-ratio profiling: cirrus case study, Atmospheric Measurement Techniques, 9, 4269–4278, https://doi.org/10.5194/amt-9-4269-2016, 2016.

Haarig, M., Ansmann, A., Althausen, D., Klepel, A., Groß, S., Freudenthaler, V., Toledano, C., Mamouri, R.-E., Farrell, D. A., Prescod, D. A., Marinou, E., Burton, S. P., Gasteiger, J., Engelmann, R., and Baars, H.: Triple-wavelength depolarization-ratio profiling of Saharan dust over Barbados during SALTRACE in 2013 and 2014, Atmospheric Chemistry and Physics, 17, 10 767–10 794, https://doi.org/10.5194/acp-17-10767-2017, 2017.

Haarig, M., Ansmann, A., Baars, H., Jimenez, C., Veselovskii, I., Engelmann, R., and Althausen, D.: Depolarization and lidar ratios at 355, 532, and 1064 nm and microphysical properties of aged tropospheric and stratospheric Canadian wildfire smoke, Atmospheric Chemistry and Physics, 18, 11 847–11 861, https://doi.org/10.5194/acp-18-11847-2018, 2018.

Hofer, J., Althausen, D., Abdullaev, S. F., Makhmudov, A. N., Nazarov, B. I., Schettler, G., Engelmann, R., Baars, H., Fomba, K. W., Müller, K., Heinold, B., Kandler, K., and Ansmann, A.: Long-term profiling of mineral dust and pollution aerosol with multiwavelength polarization Raman lidar at the Central Asian site of Dushanbe, Tajikistan: case studies, Atmospheric Chemistry and Physics, 17, 14 559–14 577, https://doi.org/10.5194/acp-17-14559-2017, 2017.

Hofer, J., Ansmann, A., Althausen, D., Engelmann, R., Baars, H., Fomba, K. W., Wandinger, U., Abdullaev, S. F., and Makhmudov, A. N.: Optical properties of Central Asian aerosol relevant for spaceborne lidar applications and aerosol typing at 355 and 532 nm, Atmospheric Chemistry and Physics, 20, 9265–9280, https://doi.org/10.5194/acp-20-9265-2020, 2020.

Holben, B., Eck, T., Slutsker, I., Tanré, D., Buis, J., Setzer, A., Vermote, E., Reagan, J., Kaufman, Y., Nakajima, T., Lavenu, F., Jankowiak, I., and Smirnov, A.: AERONET—A Federated Instrument Network and Data Archive for Aerosol Characterization, Remote Sensing of Environment, 66, 1 – 16, https://doi.org/http://dx.doi.org/10.1016/S0034-4257(98)00031-5, 1998.

Hu, Q., Wang, H., Goloub, P., Li, Z., Veselovskii, I., Podvin, T., Li, K., and Korenskiy, M.: The characterization of Taklamakan dust properties using a multiwavelength Raman polarization lidar in Kashi, China, Atmospheric Chemistry and Physics, 20, 13 817–13 834, https://doi.org/10.5194/acp-20-13817-2020, 2020.

Kemppinen, O., Nousiainen, T., and Lindqvist, H.: The impact of surface roughness on scattering by realistically shaped wavelength-scale dust particles, Journal of Quantitative Spectroscopy and Radiative Transfer, 150, 55 – 67, https://doi.org/http://dx.doi.org/10.1016/j.jqsrt.2014.05.024, 2015.

Kim, M.-H., Omar, A. H., Tackett, J. L., Vaughan, M. A., Winker, D. M., Trepte, C. R., Hu, Y., Liu, Z., Poole, L. R., Pitts, M. C., Kar, J., and Magill, B. E.: The CALIPSO version 4 automated aerosol classification and lidar ratio selection algorithm, Atmospheric Measurement Techniques, 11, 6107–6135, https://doi.org/10.5194/amt-11-6107-2018, 2018.

Mamouri, R.-E. and Ansmann, A.: Potential of polarization/Raman lidar to separate fine dust, coarse dust, maritime, and anthropogenic aerosol profiles, Atmospheric Measurement Techniques, 10, 3403–3427, https://doi.org/10.5194/amt-10-3403-2017, 2017.

Marinou, E., Amiridis, V., Binietoglou, I., Tsikerdekis, A., Solomos, S., Proestakis, E., Konsta, D., Papagiannopoulos, N., Tsekeri, A., Vlas-tou, G., Zanis, P., Balis, D., Wandinger, U., and Ansmann, A.: Three-dimensional evolution of Saharan dust transport towards Europe based on a 9-year EARLINET-optimized CALIPSO dataset, Atmospheric Chemistry and Physics, 17, 5893–5919, https://doi.org/10.5194/acp-17-5893-2017, 2017.

Mattis, I., Ansmann, A., Müller, D., Wandinger, U., and Althausen, D.: Dual-wavelength Raman lidar observations of the extinction-to-backscatter ratio of Saharan dust, Geophysical Research Letters, 29, 20–1–20–4, https://doi.org/10.1029/2002GL014721, 2002.

Miffre, A., Mehri, T., Francis, M., and Rairoux, P.: UV–VIS depolarization from Arizona Test Dust particles at exact backscattering angle, Journal of Quantitative Spectroscopy and Radiative Transfer, 169, 79 – 90, https://doi.org/http://dx.doi.org/10.1016/j.jqsrt.2015.09.016, 2016.

Müller, D., Ansmann, A., Freudenthaler, V., Kandler, K., Toledano, C., Hiebsch, A., Gasteiger, J., Esselborn, M., Tesche, M., Heese, B., Althausen, D., Weinzierl, B., Petzold, A., and von Hoyningen-Huene, W.: Mineral dust observed with AERONET Sun photometer, Raman lidar, and in situ instruments during SAMUM 2006: Shape-dependent particle properties, Journal of Geophysical Research: Atmospheres, 115, D11 207, https://doi.org/10.1029/2009JD012523, 2010.

Müller, D., Lee, K.-H., Gasteiger, J., Tesche, M., Weinzierl, B., Kandler, K., Müller, T., Toledano, C., Otto, S., Althausen, D., and Ans-mann, A.: Comparison of optical and microphysical properties of pure Saharan mineral dust observed with AERONET Sun pho-tometer, Raman lidar, and in situ instruments during SAMUM 2006, Journal of Geophysical Research: Atmospheres, 117, D07 211, https://doi.org/10.1029/2011JD016825, 2012.

Noh, Y., Müller, D., Lee, K., Kim, K., Lee, K., Shimizu, A., Sano, I., and Park, C. B.: Depolarization ratios retrieved by AERONET sun–sky radiometer data and comparison to depolarization ratios measured with lidar, Atmospheric Chemistry and Physics, 17, 6271–6290, https://doi.org/10.5194/acp-17-6271-2017, 2017.

Omar, A. H., Winker, D. M., Vaughan, M. A., Hu, Y., Trepte, C. R., Ferrare, R. A., Lee, K.-P., Hostetler, C. A., Kittaka, C., Rogers, R. R., Kuehn, R. E., and Liu, Z.: The CALIPSO Automated Aerosol Classification and Lidar Ratio Selection Algorithm, Journal of Atmospheric and Oceanic Technology, 26, 1994–2014, https://doi.org/10.1175/2009JTECHA1231.1, 2009.

Pappalardo, G., Amodeo, A., Apituley, A., Comeron, A., Freudenthaler, V., Linné, H., Ansmann, A., Bösenberg, J., D'Amico, G., Mattis, I., Mona, L., Wandinger, U., Amiridis, V., Alados-Arboledas, L., Nicolae, D., and Wiegner, M.: EARLINET: towards an advanced sustainable European aerosol lidar network, Atmospheric Measurement Techniques, 7, 2389–2409, https://doi.org/10.5194/amt-7-2389-2014, 2014.

PollyNET(2021): PollyNET lidar data base, available at: http://polly.rsd.tropos.de/, last access: 1 July, 2021.

Radenz, M., Seifert, P., Baars, H., Floutsi, A. A., Yin, Z., and Bühl, J.: Automated time–height-resolved air mass source attribution for profiling remote sensing applications, Atmospheric Chemistry and Physics, 21, 3015–3033, https://doi.org/10.5194/acp-21-3015-2021, 2021.

Saito, M., Yang, P., Ding, J., and Liu, X.: A Comprehensive Database of the Optical Properties of Irregular Aerosol Particles for Radiative Transfer Simulations, Journal of the Atmospheric Sciences, 78(7), 2089–2111, https://journals.ametsoc.org/view/journals/atsc/78/7/JAS-D-20-0338.1.xml, 2021.

Schuster, G. L., Vaughan, M., MacDonnell, D., Su, W., Winker, D., Dubovik, O., Lapyonok, T., and Trepte, C.: Comparison of CALIPSO aerosol optical depth retrievals to AERONET measurements, and a climatology for the lidar ratio of dust, Atmospheric Chemistry and Physics, 12, 7431–7452, https://doi.org/10.5194/acp-12-7431-2012, 2012.

Shin, S.-K., Tesche, M., Kim, K., Kezoudi, M., Tatarov, B., Müller, D., and Noh, Y.: On the spectral depolarisation and lidar ratio of mineral dust provided in the AERONET version 3 inversion product, Atmospheric Chemistry and Physics, 18, 12735–12746, https://doi.org/10.5194/acp-18-12735-2018, 2018.

Sinyuk, A., Holben, B. N., Eck, T. F., Giles, D. M., Slutsker, I., Korkin, S., Schafer, J. S., Smirnov, A., Sorokin, M., and Lyapustin, A.: The AERONET Version 3 aerosol retrieval algorithm, associated uncertainties and comparisons to Version 2, Atmospheric Measurement Techniques, 13, 3375–3411, https://doi.org/10.5194/amt-13-3375-2020, 2020.

Stein, A. F., Draxler, R. R., Rolph, G. D., Stunder, B. J. B., Cohen, M. D., and Ngan, F.: NOAA's HYSPLIT Atmospheric Transport and Dispersion Modeling System, Bulletin of the American Meteorological Society, 96, 2059–2077, https://doi.org/10.1175/BAMS-D-14-00110.1, 2015.

Tesche, M., Ansmann, A., Müller, D., Althausen, D., Engelmann, R., Freudenthaler, V., and Groß, S.: Vertically resolved separation of dust and smoke over Cape Verde using multiwavelength Raman and polarization lidars during Saharan Mineral Dust Experiment 2008, Journal of Geophysical Research: Atmospheres, 114, D13 202, https://doi.org/10.1029/2009JD011862, 2009a.

Tesche, M., Ansmann, A., Müller, D., Althausen, D., Mattis, I., Heese, B., Freudenthaler, V., Wiegner, M., Esselborn, M., Pisani, G., and Knippertz, P.: Vertical profiling of Saharan dust with Raman lidars and airborne HSRL in southern Morocco during SAMUM, Tellus B, 61, 144–164, https://doi.org/10.1111/j.1600-0889.2008.00390.x, 2009b.

Tesche, M., Groß, S., Ansmann, A., Müller, D., Althausen, D., Freudenthaler, V., and Esselborn, M.: Profiling of Saharan dust and biomass-burning smoke with multiwavelength polarization Raman lidar at Cape Verde, Tellus B, 63, 649–676, https://doi.org/10.1111/j.1600-0889.2011.00548.x, 2011.

Toledano, C., Torres, B., Velasco-Merino, C., Althausen, D., Groß, S., Wiegner, M., Weinzierl, B., Gasteiger, J., Ansmann, A., González, R., Mateos, D., Farrel, D., Müller, T., Haarig, M., and Cachorro, V. E.: Sun photometer retrievals of Saharan dust properties over Barbados during SALTRACE, Atmospheric Chemistry and Physics, 19, 14571–14583, https://doi.org/10.5194/acp-19-14571-2019, 2019.

Torres, B., Dubovik, O., Fuertes, D., Schuster, G., Cachorro, V. E., Lapyonok, T., Goloub, P., Blarel, L., Barreto, A., Mallet, M., Toledano, C., and Tanré, D.: Advanced characterisation of aerosol size properties from measurements of spectral optical depth using the GRASP algorithm, Atmospheric Measurement Techniques, 10, 3743–3781, https://doi.org/10.5194/amt-10-3743-2017, 2017.

Veselovskii, I., Whiteman, D. N., Korenskiy, M., Suvorina, A., and Pérez-Ramírez, D.: Use of rotational Raman measurements in multiwavelength aerosol lidar for evaluation of particle backscattering and extinction, Atmospheric Measurement Techniques, 8, 4111–4122, https://doi.org/10.5194/amt-8-4111-2015, 2015.

Veselovskii, I., Goloub, P., Podvin, T., Bovchaliuk, V., Derimian, Y., Augustin, P., Fourmentin, M., Tanre, D., Korenskiy, M., Whiteman, D. N., Diallo, A., Ndiaye, T., Kolgotin, A., and Dubovik, O.: Retrieval of optical and physical properties of African dust from multi-

wavelength Raman lidar measurements during the SHADOW campaign in Senegal, Atmospheric Chemistry and Physics, 16, 7013–7028,
https://doi.org/10.5194/acp-16-7013-2016, 2016.

Veselovskii, I., Hu, Q., Goloub, P., Podvin, T., Korenskiy, M., Derimian, Y., Legrand, M., and Castellanos, P.: Variability in lidar-derived
particle properties over West Africa due to changes in absorption: towards an understanding, Atmospheric Chemistry and Physics, 20,
6563–6581, https://doi.org/10.5194/acp-20-6563-2020, 2020.

Weinzierl, B., Ansmann, A., Prospero, J. M., Althausen, D., Benker, N., Chouza, F., Dollner, M., Farrell, D., Fomba, W. K., Freudenthaler,
V., Gasteiger, J., Groß, S., Haarig, M., Heinold, B., Kandler, K., Kristensen, T. B., Mayol-Bracero, O. L., Müller, T., Reitebuch, O.,
Sauer, D., Schäfler, A., Schepanski, K., Spanu, A., Tegen, I., Toledano, C., and Walser, A.: The Saharan Aerosol Long-range Transport
and Aerosol-Cloud-Interaction Experiment (SALTRACE): overview and selected highlights, Bulletin of the American Meteorological
Society, 98, 1427–1451, https://doi.org/10.1175/BAMS-D-15-00142.1, 2017.

Whiteman, D. N.: Examination of the traditional Raman lidar technique. I. Evaluating the temperature-dependent lidar equations, Appl. Opt.,
42, 2571–2592, https://doi.org/10.1364/AO.42.002571, 2003a.

Whiteman, D. N.: Examination of the traditional Raman lidar technique. II. Evaluating the ratios for water vapor and aerosols, Appl. Opt.,
42, 2593–2608, https://doi.org/10.1364/AO.42.002593, 2003b.

Table 1. Intensive optical properties of Saharan dust observed at Leipzig on 22–23 February (pure dust case) and 3 March 2021 (slightly polluted dust case). For comparison, the optical properties of long-range-transported Saharan dust at Barbados as observed during the SALTRACE campaign are provided, the PLDR during SALTRACE are taken from Haarig et al. (2017). SAL – Saharan Air layer, PLDR – particle linear depolarization ratio, EAE – extinction Ångström exponent, BAE – backscatter Ångström exponent

	Wvl. (nm)	22–23 Feb 2021	3 March 2021	SALTRACE
Height range		3–5 km	2–4 km	SAL
Lidar ratio	355	47±8 sr	52±8 sr	59±16 sr
	532	50±5 sr	47±5 sr	57±8 sr
	1064	63±13 sr	61±10 sr	67±15 sr[a]
Ratio of lidar ratios	355/532	0.94±0.19	1.11±0.21	1.04±0.30
	1064/532	1.26±0.29	1.30±0.25	1.31±0.32[b]
PLDR	355	0.260±0.026	0.188±0.053	0.252±0.030
	532	0.298±0.017	0.270±0.017	0.280±0.020
	1064	0.214±0.025	0.242±0.008	0.225±0.022
Ratio of PLDR	355/532	0.87±0.10	0.70±0.20	0.90±0.12
	1064/532	0.72±0.09	0.90±0.06[c]	0.80±0.10
EAE	355/532	–0.230±0.161	0.378±0.147	0.103±0.254
	532/1064	–0.054±0.178	0.034±0.082	–
	355/1064	–0.119±0.119	0.161±0.070	–
BAE	355/532	–0.087±0.446	0.111±0.276	-0.030±0.153
	532/1064	0.347±0.260	0.394±0.260	0.474±0.201
	355/1064	0.187±0.193	0.290±0.144	–

[a] Estimated using lidar and AERONET.

[b] Here the lidar ratio at 532 nm (51 sr) of the same day (20 June 2014) is used.

[c] Coincident measurements of the depolarization ratio at 532 nm (0.292) and 1064 nm are used.
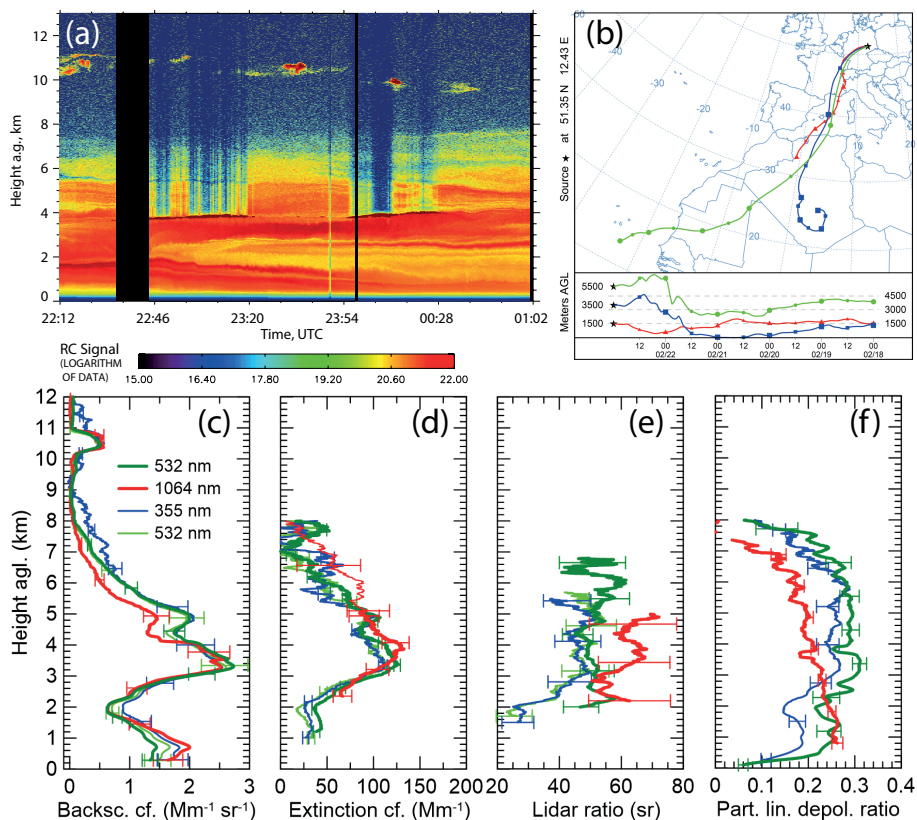
Figure 1. Saharan dust observations on 22–23 February 2021, 22:12–01:02 UTC, (a) time-height display of the 532 nm cross-polarized, range-corrected signal. During the first 20 min the depolarization ratio at 1064 nm was measured. It took around 10 min to switch to the configuration with 1064 nm extinction observation (22:45–01:02 UTC). (b) HYSPLIT backtrajectory for 23 February 2021, 00:00 UTC (<2 days from the Sahara to Leipzig). (c) Particle backscatter coefficient (570 m vertical smoothing), (d) particle extinction coefficient (950 m vertical smoothing, 2000 m (3290 m) at 1064 nm below (above) 5 km), (e) lidar ratio (1150 – 1220 m vertical smoothing, 2000 m at 1064 nm), (f) particle linear depolarization ratio (200 m vertical smoothing, 560 m at 355 nm). BERTHA provided measurements at 532 nm (dark green) and 1064 nm (red) and Arielle at 355 nm (blue) and 532 nm (light green).
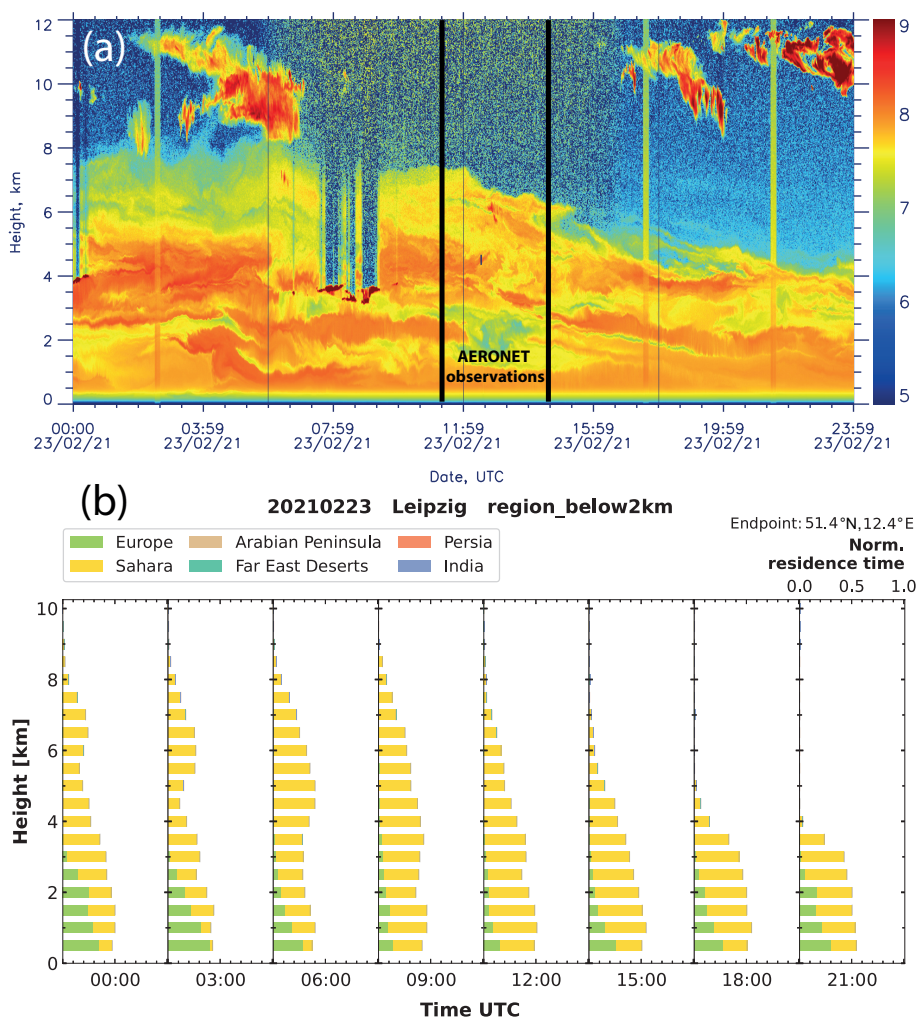
Figure 2. Development of the dust layer over Leipzig on 23 February 2021. (a) Cross-polarized, range-corrected signal at 532 nm measured with Arielle. The time frame of the five AERONET observations is marked by thick black vertical bars. (b) Source attribution in 3-hour intervals by using the method of Radenz et al. (2021). The normalized residence time of the air masses close to the ground (below 2 km height) within 10 days prior to the arrival over Leipzig at the indicated time stamps on 23 February 2021 is shown. The trajectory calculations are based on FLEXPART. The colors indicate different regions defined in Radenz et al. (2021). Here, the Saharan desert and continental Europe are relevant.
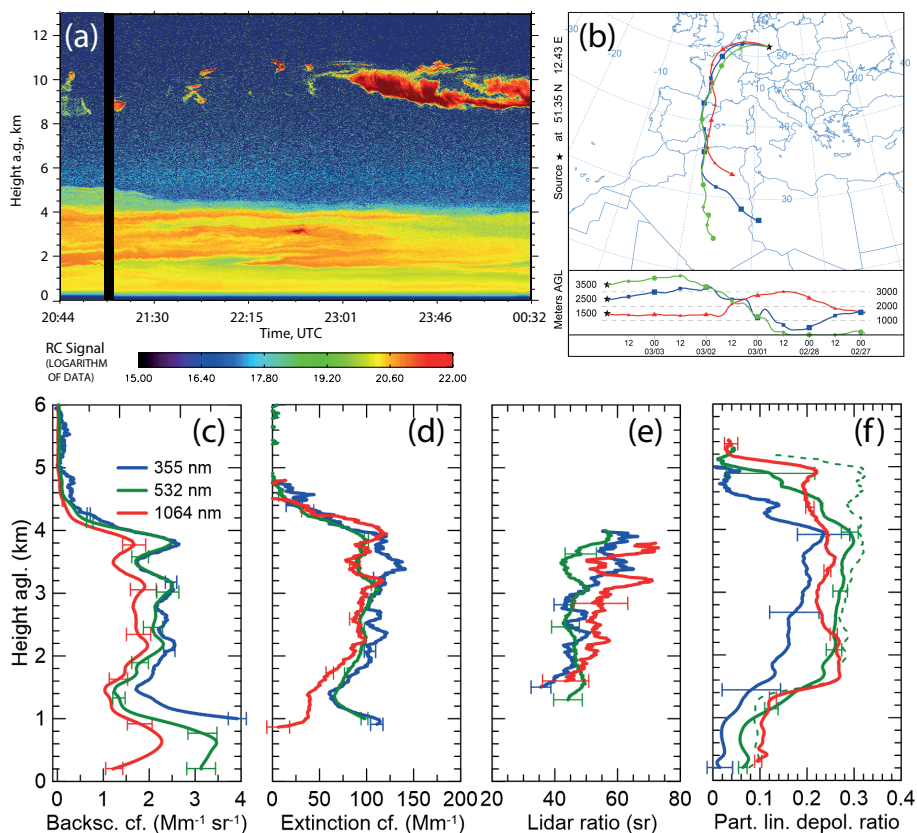
Figure 3. Same as Fig. 1, except for 3-4 March 2021, 20:44–00:32 UTC, (a) time-height display of the 532 nm cross-polarized, range-corrected signal. During the first 20 min the depolarization ratio at 1064 nm was measured. It took around 7 min to switch to the configuration with 1064 nm extinction observations (21:11-00:32 UTC). (b) HYSPLIT backtrajectory for 3 March 2021, 22:00 UTC (3–4 days). (c) Particle backscatter coefficient (202.5 m vertical smoothing), (d) particle extinction coefficient (742.5 m vertical smoothing), (e) lidar ratio (742.5 m vertical smoothing), (f) particle linear depolarization ratio PLDR (202.5 m vertical smoothing). All optical properties were measured from 21:11–00:32 UTC, except the PLDR at 1064 nm (20:44–21:04 UTC). To visualize the change in PLDR during the observation period, the PLDR at 532 nm (layer mean 0.292±0.016) measured at the same time as at 1064 nm is indicated by the green dashed line.
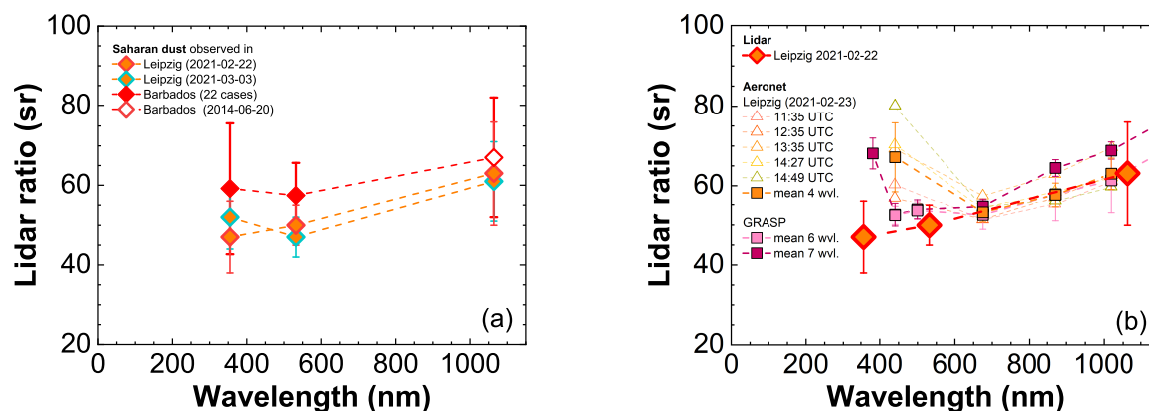
Figure 4. (a) Spectral dependence of the lidar ratio of Saharan dust observed at Leipzig and on Barbados (during SALTRACE). The lidar ratio at 1064 nm during SALTRACE (open diamond) was estimated on 20 June 2014 combining Aeronet AOT and lidar observations (see text for explanations and Mamouri and Ansmann (2017)). (b) Spectral dependence of the lidar ratio of Saharan dust observed in the night of 22–23 February 2021 compared with AERONET v3 inversion solutions for the lidar ratio on 23 February 2021. The results of the five photometer scans (open triangles) at indicated times are shown together with the mean at four wavelengths (orange squares, standard retrieval) and at six and seven wavelengths (pink and purple squares, GRASP method). The GRASP retrieval at 1640 nm (not shown) leads to lidar ratios of 94±8 (six wavelengths) and 101±4 sr (seven wavelengths) for this long wavelength.
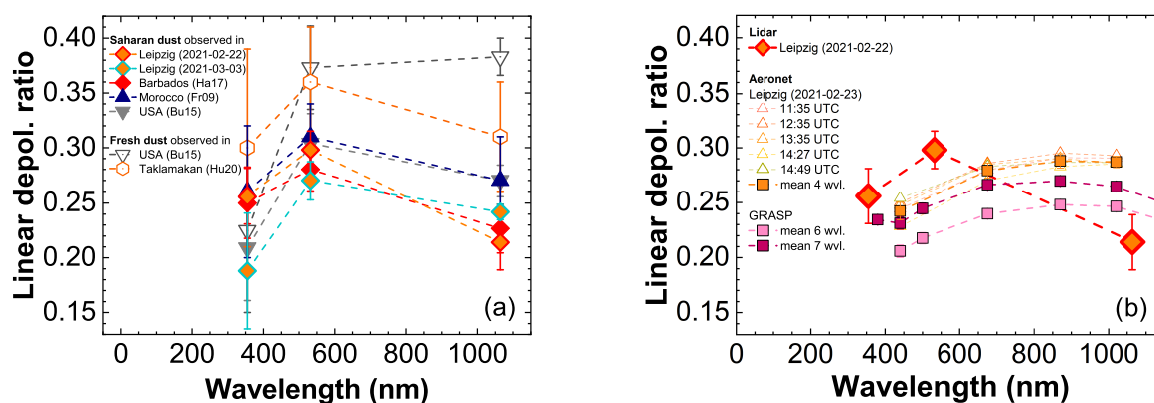
Figure 5. (a) Spectral dependence of the particle linear depolarization ratio PLDR of desert dust. The Leipzig observations are compared with triple-wavelength depolarization-ratio measurements of Saharan dust and fresh dust available in the literature (Ha17 – Haarig et al. (2017), Fr09 – Freudenthaler et al. (2009), Bu15 – Burton et al. (2015), Hu20 – Hu et al. (2020)). (b) Spectral dependence of the PLDR of Saharan dust observed in the night of 22–23 February 2021 compared with AERONET v3 inversion solutions for the PLDR on 23 February 2021. The results of the five photometer scans at indicated times are shown together with the mean at four wavelengths (orange squares, standard retrieval) and at six and seven wavelengths (pink and purple squares, GRASP method). The GRASP retrieval at 1640 nm (not shown) leads to PLDR values of 0.184±0.007 (six wavelengths) and 0.192±0.008 (seven wavelengths) for this long wavelength.